U.S. Department of Energy
Energy Efficiency and Renewable Energy
Bringing you a prosperous future where energy is clean, abundant, reliable, and affordable

Industrial Technologies Program
Industrial Materials for the Future

Final Technical Report

Inverse Process Analysis for the Acquisition of Thermophysical Data

June 2006

Principal Investigators:

Jay I. Frankel
University of Tennessee

Adrian Sabau
Oak Ridge National Laboratory

Wallace D. Porter
Oak Ridge National Laboratory

University of Tennessee

OAK RIDGE NATIONAL LABORATORY

Managed by UT-Battelle, LLC

ORNL/TM-2005/132

FINAL TECHNICAL REPORT

Project Title: Inverse Process Analysis for the Acquisition of Thermophysical Data

Award No.: DE-FC07-01ID14249

Project Period: July 1, 2001–September 30, 2004

PIs: Dr. Jay I. Frankel (UTK)
865-974-5115
vfrankel@earthlink.net

Dr. Adrian Sabau (ORNL)
865-241-5145
sabaua@ornl.gov

Wallace D. Porter (ORNL)
865-574-4460
porterwd@ornl.gov

Recipient: University of Tennessee
Mechanical and Aerospace Engineering and Engineering Science
Knoxville, TN 37996-2210

Subcontractors: Oak Ridge National Laboratory (ORNL)
Bethel Valley Road
P.O. Box 2008
Oak Ridge, TN 37831

ORNL/TM-2005/132

Inverse Process Analysis for the Acquisition of Thermophysical Data

Jay I. Frankel
University of Tennessee

Adian Sabau and Wallace D. Porter
Oak Ridge National Laboratory

June 2006

Prepared by
OAK RIDGE NATIONAL LABORATORY
P.O. Box 2008
Oak Ridge, Tennessee 37831-6283
managed by
UT-Battelle, LLC
for the
U.S. DEPARTMENT OF ENERGY
under contract DE-AC05-00OR22725

Acknowledgments and Disclaimer

Acknowledgments

This report is based upon work supported by the U.S. Department of Energy, Energy Efficiency and Renewable Energy, Industrial Technologies Program, Industrial Materials for the Future, under Award No. DE-FC07-01ID14249.

Research at Oak Ridge National Laboratory was sponsored by the U.S. Department of Energy, Office of Energy Efficiency and Renewable Energy, Industrial Technologies Program, under contract DE-AC05-00OR22725 with UT-Battelle, LLC. The authors wish to thank Peter Angelini, Oak Ridge National Laboratory, for project guidance and review.

Contents

List of Figures

List of Tables

Abbreviations and Acronyms

DSC	differential scanning calorimeter
DTA	differential thermal analysis
ID	inner diameter
LVDT	linear variable differential transducer
NIST	National Institute of Standards and Technology
OD	outer diameter
ORNL	Oak Ridge National Laboratory
RBF	radial basis function
SRM	standard reference material
UTK	University of Tennessee at Knoxville

1. Executive Summary

One of the main barriers in the analysis and design of materials processing and industrial applications is the lack of accurate experimental data on the thermophysical properties of materials. To date, the measurement of most of these high-temperature thermophysical properties has often been plagued by temperature lags that are inherent in measurement techniques. These lags can be accounted for with the appropriate mathematical models, reflecting the experimental apparatus and sample region, in order to deduce the desired measurement as a function of true sample temperature. Differential scanning calorimeter (DSC) measurements are routinely used to determine enthalpies of phase change, phase transition temperatures, glass transition temperatures, and heat capacities. DSC data have also been used to estimate the fractional latent heat release during phase changes. In the aluminum, steel, and metal casting industries, predicting the formation of defects such as shrinkage voids, microporosity, and macrosegregation is limited by the data available on fraction solid and density evolution during solidification. Dilatometer measurements are routinely used to determine the density of a sample at various temperatures.

An accurate determination of the thermophysical properties of materials is needed to achieve accuracy in the numerical simulations used to improve or design new material processes. In most of the instruments used to measure thermophysical properties, the temperature is changed according to instrument controllers and there is a nonhomogeneous temperature distribution within the instrument. To further complicate matters, the sample temperature cannot be measured directly: temperature data are collected from a thermocouple that is placed at a different location than that of the sample. Consequently, there is a time (or temperature) lag of the sample temperature related to factors such as heating/cooling rate, sample mass, and thermal contact resistance between the sample and sensor. By performing a computational analysis of the measurement process, the lag can be estimated and its effect can be taken into account in determining the desired thermophysical properties. This would significantly improve the quality of the data as a function of sample temperature and not thermocouple temperature.

The goal of this project was to extend the utility, quality and accuracy of two types of commercial instruments — a differential scanning calorimeter (DSC) and a dilatometer — used for thermophysical property measurements in high-temperature environments. In particular, the quantification of solid fraction and density during solidification was deemed of critical importance. To accomplish this project goal, we redesigned sample holders and developed inverse mathematical methods to account for system lags. The desired property could then be correlated to the proper sample temperature based on using remote temperature measurements.

1.1 Differential Scanning Calorimeter

For the NETZSCH DSC 404C instrument with a high-accuracy heat capacity sensor, a mathematical model was developed by assuming that each component was isothermal and that the heat transfer among components occurred by conduction and radiation. Model parameters included effective conduction time constants and radiation time constants. Several model cases were investigated to assess the effect of heat transfer interactions. New features that have not been considered in previous DSC models were included in the present study. These new features included (*a*) considering the sensor platform, (*b*) accounting for the heat loss through the stem, and (*c*) considering the lag between furnace temperature and set point temperature. Comparisons with experimental results showed that temperature lags in heat flux DSC instruments could be determined by performing a heat transfer

analysis based on a comprehensive model. The proposed mathematical model yielded accurate results over a wide temperature range during heating and cooling regimes.

This project pioneered the use of inverse analysis for DSC data. However, traditional inverse analysis methods yielded limited success with the DSC system. Therefore, we used a direct analysis technique. The direct analytical model accurately described the experimental data. In addition, this method is easier to implement and more user-friendly. *The DSC model has been validated for pure aluminum and successfully applied to study the commercial aluminum alloy A356.*

1.2 Dilatometer

The induced thermal lag in the Theta Industries dual push-rod horizontal dilatometer is apparent owing to the distance of the thermocouple from the actual sample. In a near steady-state mode of operation, this apparent problem is minimal. However, in a transient situation, where the density is varying as a function of time, the temperature output from the remote temperature sensor must be adjusted in order to reflect the sample temperature. Because of its complicated geometry, the original insert region of the dilatometer did not permit an analytic analysis.

Therefore, the conventional push-rod dilatometer insert (sample holder) was modified significantly to allow an accurate correlation of the measured density to the predicted sample temperature of alloys in the phase-change regime. This new configuration made use of a standard furnace assembly; however, the specimen was symmetrically encased in a well-instrumented cylindrical graphite shell. This new insert was designed, fabricated, instrumented, calibrated, and tested. It was demonstrated, using an array of high-precision thermocouples, that a nearly uniform temperature distribution existed in the sample holder (i.e., no temperature gradient at the heating rates of interest). The combination of system geometry and high-conductivity sample holder material promoted the development of a simplified but highly effective inverse heat transfer model. The prediction of this model properly correlated the measured density in the phase change regime to that of the actual sample temperature based on using remote, sample-holder temperature measurements. Preliminary results using aluminum A356 provide insight into the proposed configuration. It was demonstrated that accurate modeling of the solid fraction was important for accounting for thermal lags in the phase-change regime. Additionally, the average heat transfer coefficient during phase change was also calculated and compared to existing results. Both results were deemed accurate and significant.

1.3 Technology Transfer

The algorithm developed for establishing sample temperature in the DSC and the newly designed sample holder with inverse analysis for the dilatometer present two potential products for measurement device manufacturers. The dissemination of the findings in conference and archival publications provides opportunities for readers to contact Oak Ridge National Laboratory (ORNL) and the University of Tennessee at Knoxville (UTK).

As an additional opportunity to validate the results of the modeling and improved experimental procedures determined from this project, the computational approach was utilized in another project, “Predicting Pattern Tooling and Casting Dimensions for Investment Casting” (DE-FC36-01ID14003), in order to obtain optimal thermophysical properties for aluminum alloy A356. NETZSCH, Inc., one of instrument manufacturers, expressed interest in the computer program. The techniques developed in the program were documented in several publications that were sent to the instrument manufacturers.

1.4 Recommendations

This project was a feasibility study. For technology dissemination, it is now recommended that a new project should be set up and conducted in collaboration with instrument suppliers and a team of users.

2. Introduction

Accurate thermophysical properties [1–11] are necessary for a wide application base and thus are inherently crosscutting in nature. Several industries will derive benefits from this investigation. These include the metal casting (die casting, lost foam, sand casting, etc.), aluminum (die casting, continuous casting, etc.), steel (continuous casting, alloy design), and glass industries. The general intent of this investigation was to develop a methodology for augmenting accurate thermophysical properties to improve materials design and optimization, reduce scrap material, reduce downtime, increase process productivity by permitting rapid changes between material types, and improve properties of products by decreasing hot tearing defects, improving strength, reducing porosity defects, and improving fracture resistance. These concepts all require accurate characterization of material properties.

The *metal casting industry* [5] is a fundamental building block for other U.S. industries. Castings appear in more than 90% of all manufactured goods and in 100% of all manufacturing machinery. For example, the multibillion-dollar metal casting industry serves the motor vehicle industry, industrial machinery manufacturers, and electrical-power equipment industries. The competitiveness of all these industries relies on techniques for the improvement of products and processes. Foreign competition has greatly increased over the past decade. The current project impacts the following areas identified as high priorities in the Metalcasting Industry Technology Roadmap [5]:

1. development of improved techniques and software for evaluating key thermophysical properties [5, p. 3];
2. the potential for standardizing material properties evaluation [5, p. 10];
3. fostering material development and reducing design time [5, p. 10];
4. improving existing tools and processes in the near, mid, and long term [5, pp. 11, 13, 14];
5. improving accurate evaluation of material properties [5, p. 17].

Item 5 has been identified by the metal casting roadmap as a technology barrier: “The single most critical barrier to improving the variety, integrity and performance of castings is the lack of fundamental knowledge of material properties” [5, p. 17].

The *aluminum industry* has identified several key issues related to material properties [6,7]. The unique properties of aluminum alloys (light weight, high strength, good resistance to corrosion) offer several advantages over conventional ferrous-type materials. As noted in the Aluminum Industry Technology Roadmap [6, p. 5], aluminum is electricity-intensive, and thus, recycling of scrap aluminum is advantageous. A number of technology barriers have been identified [6, p. 7]. In particular, a highest priority involves “fully understanding the relationship of aluminum alloy and processing and its effect on microstructure and properties” [6, p. 37]. Again, the common theme of thermophysical (and mechanical) properties represents a key ingredient in the roadmap.

Steel is a “cutting edge” material [8, p. 1], and the *steel sector* produces approximately 100 million tons of steel annually. Several technological challenges have been identified including the fact that the “prediction accuracy of heat treatment and quenching models is limited by lack of reliable, material-specific input data” [8, p. 35]. In addition, “material property characterization and the development of new coatings have significant importance in rolling and finishing technologies of the future” [8, p. 38].

The *glass sector* [9] plays a fundamental role in a variety of consumer products owing to its unique attributes, which include transparency (in the visible portion of the spectrum), chemical durability, optical properties, low cost, and recyclability. The Glass Technology Roadmap Workshop noted that a priority associated with technological barriers in achieving production efficiency goals involves the "the need for better material property data" [9, p. 13]. It is also noted that an important near-term research need involves the "capability for systematic measurement of physical properties as a function of temperature" [9, p. 16].

It is evident from a review of the needs of these four industrial sectors that accurate material properties involving both thermal and mechanical character are still required. Several industries associated with these sectors will derive benefits from this project. Table 2.1 summarizes the energy cost savings that could be associated with these industries.

Table 2.1. Energy cost savings impact by year 2020

Vision industry	Energy cost savings (million $/year)
Metal	24
Glass	30
Other manufacturers	40
Total	94

Table 2.2 presents energy savings for industries based on an impact analysis using the Energy Savings Worksheet developed by the U.S. Department of Energy's (DOE's) Office of Technologies [10]. The results show that significant benefits will be achieved using accurate thermophysical properties in product design. These results were based on the following assumptions:

- improvement in the process heating requirements of the metal and glass industries, 0.5%;
- improvement in the process heating requirements of other manufacturing industries, 0.6%;
- annual growth rate of technology, 2%;
- ultimate potential market share, 90%;
- likely market share, 90%;
- first year of introduction, 2005.

The process heating information, including total energy used in each industry and the fraction of energy type (electricity, natural gas, oil, and coal), was obtained from the Process Heating Technology Roadmap [11].

Table 2. 2. Results of energy benefits impact analysis: impact by 2020

Vision industry	Energy savings				
	Electricity (billion kWh)	Gas (billion ft^3)	Oil (million barrels)	Coal (million tons)	Total energy savings (trillion BTU)
Metal	0.10	3.6	0.04	0.02	5
Glass	0.14	4.0	0.04	0.02	6
Other manufacturers	0.09	2.2	0.05	0.015	6
Total savings	0.33	9.8	0.13	0.055	17

Table 2. 3 presents environmental benefits estimated to result from the energy savings associated with the use of improved techniques for data acquisition of thermophysical properties in the material processing and industrial applications. The data in this table highlight two gases: CO_2 and NO_x .

Table 2.3. Environmental benefits: impact by 2020

Manufacturer	Environmental savings (thousand tons/year)	
	CO_2	NO_x
Metal	80	0.70
Glass	96	0.80
Other manufacturers	60	0.55
Total	236	2.05

3. Background

The present state of the art for DSCs and dilatometers can be divided into domestic technology and worldwide technology. A survey of domestic thermal analysis instrument vendors indicates an active interest in recognizing and treating instrumental effects caused by instrument time constants and thermal resistance in DSC instruments. For example, TA Instruments has a newly released low-temperature-range heat-flux-type DSC whose sensor has been redesigned to allow determination of the contact resistance between pans and sensor plates. A third thermocouple, located on the sensor plate between the sample and reference positions, has been added in an attempt to account for asymmetry of the sensor. This instrument is an improvement in technology but can be used only up to about 700°C. Moreover, some of the assumptions made involve the use of crimped aluminum pans. While these conditions meet the needs of the polymer field targeted for this instrument, the instrument does not satisfy the requirements of the metal casting community.

The domestic manufacturers of dilatometers are currently not addressing the issue of instrumental temperature effects or the need for high-precision molten metal density measurements. The findings of this project represent an important advancement that may later be incorporated into new a new generation of instruments accessible by industry.

The status of DSC technology development worldwide is similar to that in the United States. Interest in the problem of instrumental effects is demonstrated by the efforts of NETZSCH Instruments and Mettler. NETZSCH has developed an offline software module that will adjust, or "desmear," a DSC peak to remove or minimize instrument effects. This algorithm however, does not account for the possibility that contact resistances could change as a function of temperature. Mettler has developed a hardware approach by using a thermopile sensor. In this sensor, the time constant and thermal resistances can be improved without sacrificing sensor sensitivity. As with TA Instrument's DSC, the Mettler sensor has maximum temperature limitations, in this case below 1000°C. NETZSCH appears to be the only dilatometer manufacturer addressing the need for molten metal density measurements utilizing dilatometers. The company has a software module that makes density calculations, but no attempt is made to correct for instrument temperature effects.

One of the main barriers in the analysis and design of materials processing and industrial applications is the lack of accurate thermophysical property data as obtained from conventional instruments. To date, the measurement of most high-temperature thermophysical properties is often plagued by thermal (time/temperature) lags and poor thermal modeling that does not properly take into account thermal resistance in the physical network. This thermal lag is very undesirable, especially at elevated temperatures, where thermal radiation represents a significant mode of heat transfer. Poor accounting of the physics leads to significant errors in the interpreted measurements. These lags are inherent to the measurement arrangement since (*a*) the sample temperature cannot usually be measured directly and is normally acquired by use of a thermocouple located at a distant location, and (*b*) there is a nonhomogeneous temperature distribution within the instrument.

The goal of this project was to improve the acquisition of data on thermophysical properties such as solid fraction and density during solidification by concurrently developing realistic thermal models and redesigning sample holders that promote simplification in the models. This concept permits the performance of a computational analysis of the measurement process that will account for time lags and thermal resistance. This approach translates to correlating the desired property with the true sample temperature.

The approach of this project focused on analyzing the measurement of thermophysical properties taken by the DSC and dilatometer instruments at high temperature (see Table 3.1). In this project, we developed new computational methodologies and measurement procedures to acquire accurate thermophysical data as required for modeling the transport processes associated with solidification. The results of the project should have a beneficial impact on the industries we noted previously.

Table 3.1. Instruments investigated and thermophysical properties considered for this project

Instrument	Measured value	Property determined by analysis
DSC	Temperature of phase changes, latent heat, specific heat	Solid fraction
Dual push-rod dilatometer	Bulk density and temperature	Density of solid and liquid phases

The joint ORNL and UTK effort involved the expertise, in particular, of Dr. A. Sabau (industrial heat transfer) and W. D. Porter (experiment and instrumentation of both the DSC and the dilatometer) from ORNL and of Professor J. I. Frankel (heat transfer, inverse analysis, and numerical methods) from UTK. The project lead responsibilities were divided with ORNL responsible for the DSC portion and UTK for the dilatometer, though complete interaction among the members were called for during the investigative period, as indicated in Figure 3.1.

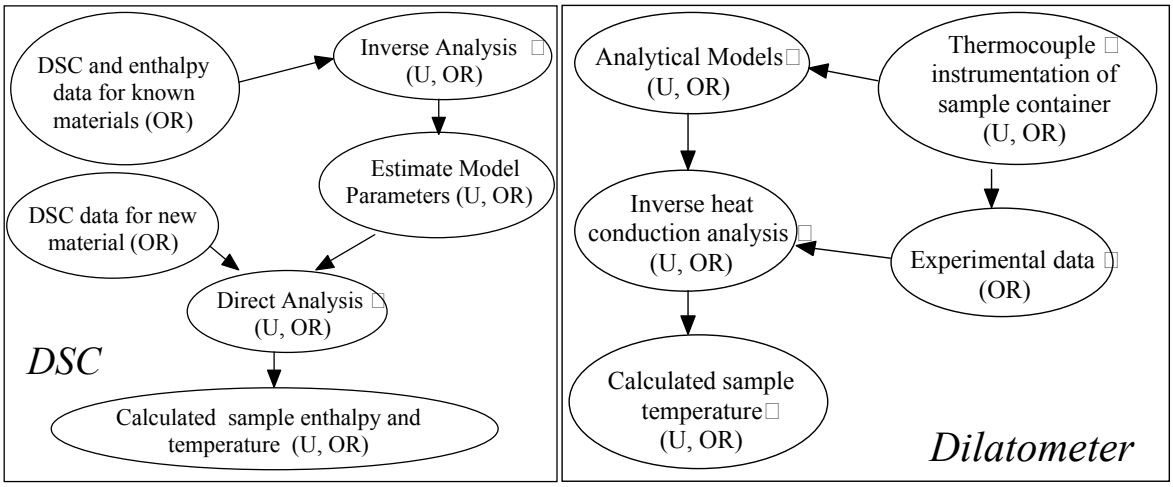

Figure 3.1. Flow and responsibilities associated with the project. *Abbreviations:* OR = ORNL, U = UTK.

The task breakdown for the project is described below.

Task 1: Develop Analytical Models for DSC

1.1 Develop a heat transfer model by considering all heat-transfer mechanisms between the system components (UTK, ORNL)
1.2 Identify temperature-dependent model parameters and their constitutive equations (UTK, ORNL)
1.3 Develop and implement "parameter estimation" inverse models (UTK)
1.4 Validate the inverse algorithm by using other experimental and numerically obtained solid fraction (UTK)

Task 2: Develop Analytical Models for Dilatometer

2.1 Design thermocouple instrumentation for sample container (UTK, ORNL)
2.2 Develop inverse model for container and sample (UTK, ORNL)
2.3 Implement "function estimation" inverse methodology (UTK)
2.4 Validate the inverse algorithm (UTK)

Task 3: Conduct DSC and Dilatometry Measurements

3.1 Provide additional thermocouple instrumentation for sample container (ORNL)
3.2 Calibrate instruments (ORNL)
3.3 Perform DSC measurements at different cooling/heating rates (ORNL, UTK)
3.4 Perform dilatometry measurements at different cooling/heating rates (ORNL, UTK)

Task 4: Experimentally Validate Proposed Methodologies

4.1 Determine new property data by performing inverse analyses (ORNL, UTK)
4.2 Assess accuracy of new property data by comparison with known data (ORNL, UTK)
4.3 Perform controlled casting experiments and collect data needed for data validation (ORNL)
4.4 Perform numerical simulation of casting experiments using the new property data (ORNL)
4.5 Assess the accuracy of the new property data by comparing cooling curve and shrinkage predictions with experimental data (ORNL, UTK)

Task 5: Write Report on Experimental and Computational Procedures

5.1 Develop flow chart of computational methodologies developed (UTK, ORNL)
5.2 Write experimental procedures for DSC and dilatometer operation (UTK, ORNL)
5.3 Complete final report (UTK, ORNL)

4. Results and Discussion

This project involved two measurement instruments. Section 4.1 presents the results from the DSC portion of the effort, while Section 4.2 describes the dilatometer aspect of the project.

4.1 Differential Scanning Calorimeter (DSC)

Because of the similarities between the differential thermal analysis (DTA) and DSC instruments, the methodology proposed by Gray [12] to describe heat flow in DTA cells has been widely adopted for the study of DSC instruments. This methodology has been used with little change even in more recent studies for determining solid fraction distribution as a function of temperature for commercial alloys [13]. Dong and Hunt [14] developed an analytical model for the DSC heat flux instrument by considering that the instrument can be represented by a certain number of regions of uniform temperatures. However, that model included some heat transfer features that do not exist in the instrument, such as conduction paths between the sample plates and the furnace.

Speyer [15] used simplex algorithms to desmear the raw signal from DTA/DSC peaks. Kempen et al. [16] modeled the NETZSCH DSC 404C heat flux instrument using the DTA methodology. In their approach, a methodology was proposed for determining model parameters by employing DSC measurements for two known sample materials, one with a smooth specific heat capacity and the other one with a sharp transition. The heat transfer mechanisms were oversimplified — e.g., only the plates and the pans were considered in the model and a conduction path between the sample plates and the furnace were considered. In order to calibrate the thermocouple, a temperature shift of the thermocouple was introduced, while the temperature lag between the sample and the sample plate was not accurately determined, since the sample container was assumed to have the same temperature as the sample itself.

The main reason for carrying out the DSC portion of the current project was to enable more accurate measurement of the fraction latent heat of materials.

4.1.1 Data Acquisition

The data provided by the DSC heat flux instrument were the voltage difference between the two thermocouples and the temperature of one thermocouple. The voltage difference is proportional to the temperature difference between the thermocouples. After post-processing of the raw signal according to the directions of the instrument manufacturer, the heat flow between the sample and the reference side of the instrument was obtained; see Figure 4.1(a). The data shown in Figure 4.1(a) was obtained with a Stanton-Redcroft DSC instrument. The fractional latent heat release was determined by integrating partial areas between the baseline and the DSC curve [Figure 4.1(b)]. For most alloys, the fractional latent heat released during solidification correlated directly to the fraction solid. At times, the data generated could not be used because of large discrepancies between the values for solidus, eutectic, and liquidus temperatures.

The liquidus and solidus temperatures were determined from the DSC measurements performed during cooling and heating, respectively. Due to the instrument time constant effects, the solidus was not determined from DSC measurements conducted upon cooling. Thus, the fractional latent heat (or solid fraction), which was determined from DSC measurements upon cooling, extended to lower temperatures than the solidus. These data at temperatures near the solidus were very important for the prediction of casting defects such as microporosity and hot tearing, which occur when low amounts of

liquid fraction are present in the alloy. In order to obtain more accurate data on fraction solid versus temperature, an analysis of the DSC system was made as part of the current project.

The NETZSCH DSC 404C instrument, with a high-accuracy heat capacity sensor, was considered in this project. Figure 4.2(a) shows the sensing unit. The individual components of the DSC sensing system are identified and a schematic of the sensing unit is shown in Figure 4.2(b). Based on the construction of the DSC sensing system, the following parts were identified: (1) sample plate, (2) reference plate, (3) container, (4) sample container, (5) reference container, (6) alumina disk, and (7) sample. The sensing unit is held by a stem and is placed into a furnace. The furnace inner diameter is very close to that of the alumina disk. Sometimes, a sample of known material is placed in the reference container.

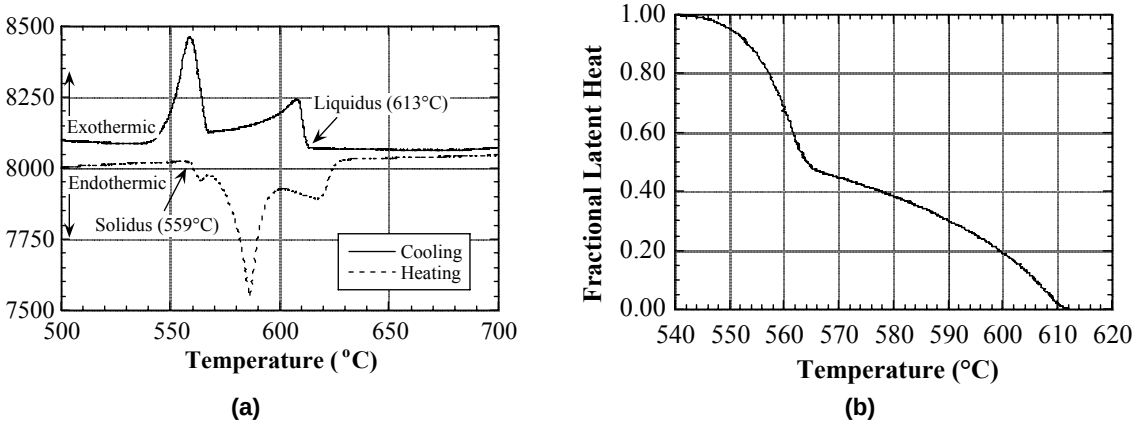

Figure 4.1. Data on A356 aluminum alloy. (*a*) DSC data indicating that liquidus, eutectic, and solidus temperatures are 613, 574, and 559°C, respectively. (*b*) Fractional latent heat determined using DSC at cooling. The fraction latent heat extends to 545°C, well below that of the solidus.

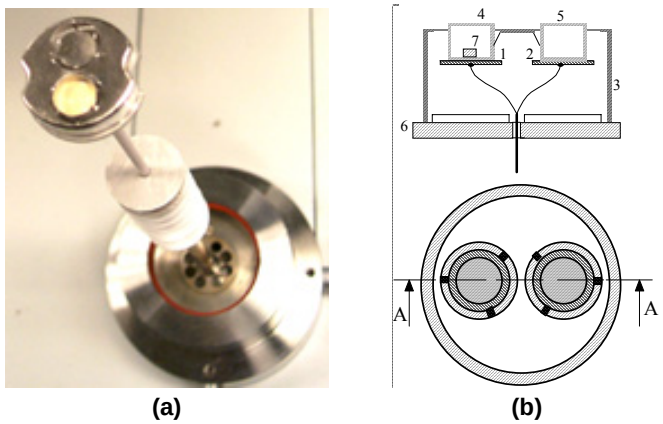

Figure 4.2. Cell mounting for typical heat flux–type DSC head system used for high-temperature applications. (a) Photo; (b) schematic of DSC sensing system.

4.1.2 Analytical Model

A system of nonlinear ordinary differential equations accounts for the conduction and radiation heat transfer within the instrument. Temperatures are normalized with respect to the initial temperature, i.e., $y = T/T_o$. The most complex model, which includes all the heat transfer interactions between different components of the DSC sensing unit, is shown in Table 4.1. The mathematical model is based on the assumption that each component is isothermal and that the heat transfer among components occurs by conduction and radiation. The thermal resistances in the system are represented by effective conduction time constants, τ_C, and radiation time constants, τ_R.

Table 4.1. Analytical model of the DSC instrument

DSC assembly part	Dimensionless variable	Equation
Furnace	y_0	$\frac{dy_0}{dt} = \frac{y_P - y_0}{\tau_{CF}}$
Reference plate	y_1	$c_1 \frac{dy_1}{dt} = \frac{y_3 - y_1}{\tau_{C1}} + \frac{y_3^4 - y_1^4}{\tau_{R1}} + \frac{y_4 - y_1}{\tau_{C3}} + \frac{y_6^4 - y_1^4}{\tau_{R4}}$
Sample plate	y_2	$c_2 \frac{dy_2}{dt} = \frac{y_3 - y_2}{\tau_{C2}} + \frac{y_3^4 - y_2^4}{\tau_{R1}} f_1 + \frac{y_5 - y_2}{\tau_{C4}} + \frac{y_6^4 - y_2^4}{\tau_{R4}} f_1$
Container	Y_3	$c_3 \frac{dy_3}{dt} = \frac{y_1 - y_3}{\tau_{C1}} f_2 + \frac{y_2 - y_3}{\tau_{C2}} \frac{f_2}{f_1} + \frac{y_0^4 - y_3^4}{\tau_{R2}} + \frac{y_6^4 - y_3^4}{\tau_{R5}}$
Reference container	Y_4	$c_4 \frac{dy_4}{dt} = \frac{y_1 - y_4}{\tau_{C3}} f_3 + \frac{y_0^4 - y_4^4}{\tau_{R3}} + \frac{y_8 - y_4}{\tau_{C5}} f_{10} + \frac{y_5^4 - y_4^4}{\tau_{R8}}$
Sample container	y_5	$c_5 \frac{dy_5}{dt} = \frac{y_2 - y_5}{\tau_{C4}} f_4 + \frac{y_0^4 - y_5^4}{\tau_{R3}} f_5 + \frac{y_7 - y_5}{\tau_{C6}} f_8 + \frac{y_4^4 - y_5^4}{\tau_{R8}} f_5$
Disk	y_6	$c_6 \frac{dy_6}{dt} = \frac{y_3^4 - y_6^4}{\tau_{R5}} f_6 + \frac{y_0^4 - y_6^4}{\tau_{R6}} f_7 + \frac{y_{sce} - y_6}{\tau_{C7}} + \frac{y_{sce}^4 - y_6^4}{\tau_{R7}}$
Sample material	y_7, f_{S7}	$c_7 \frac{dy_7}{dt} + c_{f7} \frac{df_{S7}}{dt} = \frac{y_5 - y_7}{\tau_{C6}} f_9,$
Reference material	y_8	$c_8 \frac{dy_8}{dt} = \frac{y_4 - y_8}{\tau_{C5}} f_{11}$

An analysis of the model is presented in later sections with the aim of formulating one of the simplest models that can qualitatively reproduce all the typical features of a DSC signal.

In Table 4.1, $c_k = C_p^k(y_k) / C_p^k(1)$. $c_{f7} = -L_7 / C_p^7(1) T_0 + y_m \left(C_p^{7,L} - C_p^{7,S}\right) / C_p^7(1)$, where L_7 is the latent heat of the sample material, $C_p^{7,L}$ is the specific heat of the liquid metal at the melting point, and $C_p^{7,S}$ is the specific heat of the pure metal in the solid state at the melting point. Since the

controller thermocouple was located away from the furnace walls, a temperature lag between the controller temperature and furnace wall temperature was considered.

The set point temperature was defined as the temperature set by the operator and was usually a linear variation in time given by the constant heating or cooling rate. In the approach described above, numerous parameters had to be determined. In order to describe the system with minimal components, an analysis was required to ascertain the effect of including each of the components and its associated model parameters. Some of these physical parameters could be determined with the aid of special experiments, while others were determined with the aid of an inverse parameter-estimation analysis.

The components have the following mass (in grams): $m_1 = 0.103$, $m_2 = 0.103$, $m_3 = 1.21$, and $m_6 = 1.53$. For latent heat measurements, the reference and sample containers were made of alumina, and their masses were $m_4 = 0.2481$ and $m_5 = 0.2437$, respectively. When platinum containers were used, their masses were $m_4 = 0.2596$, $m_5 = 0.258$. The mass factors in the analytical DSC model were given as $f_1 = m_1/m_2$, $f_2 = m_1/m_3$, $f_3 = \frac{m_1 C_p^1(1)}{m_4 C_p^4(1)}$, $f_4 = \frac{m_2 C_p^2(1)}{m_5 C_p^5(1)}$, $f_5 = m_4/m_5$, $f_6 = \frac{m_3 C_p^3(1)}{m_6 C_p^6(1)}$, $f_7 = 1$, $f_8 = 1$, $f_9 = \frac{m_5 C_p^5(1)}{m_7 C_p^7(1)}$, $f_{10} = 1$, $f_{11} = \frac{m_4 C_p^4(1)}{m_8 C_p^8(1)}$.

During a DSC run, a temperature and differential voltage were acquired. The differential voltage was converted to the differential temperature between the sample side and reference side, $T_s - T_r$. Thus, the model was developed and validated in two steps:

1. model parameters for the measured reference temperature, T_r;
2. model parameters for the differential temperature, $T_s - T_r$.

4.1.3 Results for Reference Temperature

A comprehensive DSC model was formulated as described in previous sections (see Table 4.1). Since the model includes all the heat transfer interactions between different components of the DSC sensing unit, it had a relatively large number of parameters. In this section, we present numerical simulation results for several simplified models that were obtained by excluding some features of the detailed model. The computational results were compared against experimental data for empty containers — i.e. without sample and reference materials — and for pure aluminum in order to assess which were the most critical model features in order to qualitatively reproduce all the typical features of a DSC signal. Initially, experiments were performed at heating rates of 20°C/min from room temperature until the set point reached a temperature of 1073 K, following by cooling at a rate of −20°C/min.

The several cases considered are identified in Table 4.2. For each case, the parameters were varied such that a good agreement with experimental results was attained for as large a temperature domain as possible. The information on conduction parameters and relative range between radiation parameters presented in previous sections was used to limit the choice of parameters and their variation range. The representative parameters for each case are shown in Table 4.3. A variable considered for comparison was either the ratio between the reference plate temperature and the set point temperature, T_r/T_p, or the difference between the sample plate temperature and the reference plate temperature, $T_s - T_r$.

Table 4.2. Cases considered for numerical simulations

	Features of the DSC model			
Case ID	Furnace set point lag	Alumina disk	Stem heat loss	Radiation between containers
1	—	—	—	—
2	Y	—	—	—
3	Y	—	—	—
4	Y	Y	—	—
5	Y	Y	—	—
6	Y	Y	Y	—
7	Y	Y	Y	Y

Table 4.3. Time constants (in seconds) for cases considered for numerical simulations

Case ID	Radiation parameters							Furnace	Stem parameters	
	τ_{R1}*	τ_{R2}	τ_{R3}	τ_{R4}	τ_{R5}	τ_{R6}	τ_{R8}	τ_{CF}	τ_{C7}	τ_{R7}
1	650	3000	1500	—	—	—		—	—	—
2	650	1000	1000	—	—	—		40	—	—
3	650	2000	2000	—	—	—		40	—	—
4	650	1000	680	220	200	6300		40	—	—
5	650	1000	680	20	200	6300		40	—	—
6	650	1000	680	220	200	6300		40	2000	30000
7	650	1000	680	220	200	6300	4000	40	2000	30000

*τ_{R1} is not important to T_R results. The following conduction parameters were considered: $\tau_{C1} = \tau_{C2} = 3.3$, $\tau_{C3} = \tau_{C4} = 0.01$, $\tau_{C5} = 1$, $\tau_{C6} = 10$ s.

For the first case, a good agreement between numerical and computational results was obtained only in the low-temperature domain [Figure 4.3(a)]. We found that including the furnace set-point lag feature yielded more realistic variation in the reference temperature [Figure 4.3(b)]. The difference between T_r/T_p at cooling and heating was governed by τ_{CF}, and a value for τ_{CF} of 40 s was found to be the most appropriate. Figure 4.3(b) shows results for the two extreme values of τ_{R2}. For case 3, the parameter τ_{R3} was varied accordingly in order to improve the agreement. At low values of τ_{R2} and τ_{R3} (i.e., case 2) excellent agreement was observed again for the low-temperature domain. In order to improve the agreement at high temperatures, higher values of τ_{R2} and τ_{R3} were required (i.e., case 3). However, the numerical results had an unacceptable deviation from the experimental results at intermediate temperature ranges (between 360 and 550 K). For the results presented in Figure 4.3, the alumina disk component was excluded. When the alumina disk was included in the model, the agreement with experimental results was improved at those temperature ranges where the previous case three lacked good agreement [17].

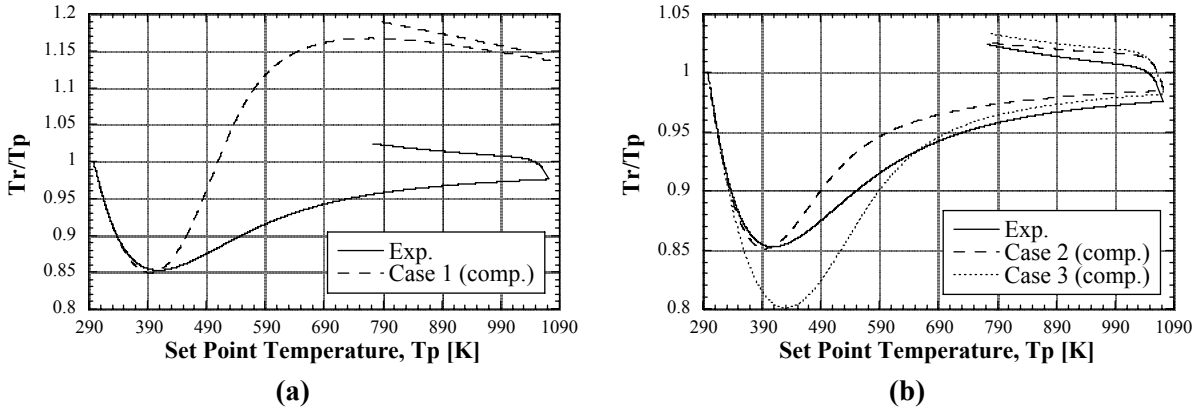

Figure 4.3. Ratio between the reference plate temperature and set point temperature for (*a*) case 1 and (*b*) cases 2 and 3 (Table 4.3).

Next, we considered the heat transfer losses through the stem that supports the alumina disk [17]. We concluded that inclusion of this effect was important, since the mounting end of the stem was held at constant temperature of about 340 K using additional water cooling. Good agreement at all temperature ranges was obtained when this feature was considered [see Figure 4.4(a)].

To test the proposed methodology, we conducted experiments at other heating and cooling rates [see Figure 4.4(b)]. The model parameters were those considered for case 6. These additional subcase simulations were labeled with the corresponding heating and cooling rates. In all the subcases considered, the heating rates were 20°C/min until the set point reached 873 K. The subcases were labeled with *M/N,* where *M* = 20 represents the first heating rate and *N* the corresponding second heating rate in degrees Celsius per minute (e.g., Exp. 20/20). Cooling was performed with the same rate as that of the last heating segment. Only the high-temperature domain is shown in Figure 4.4(b). The agreement on heating for all heating rates was excellent.

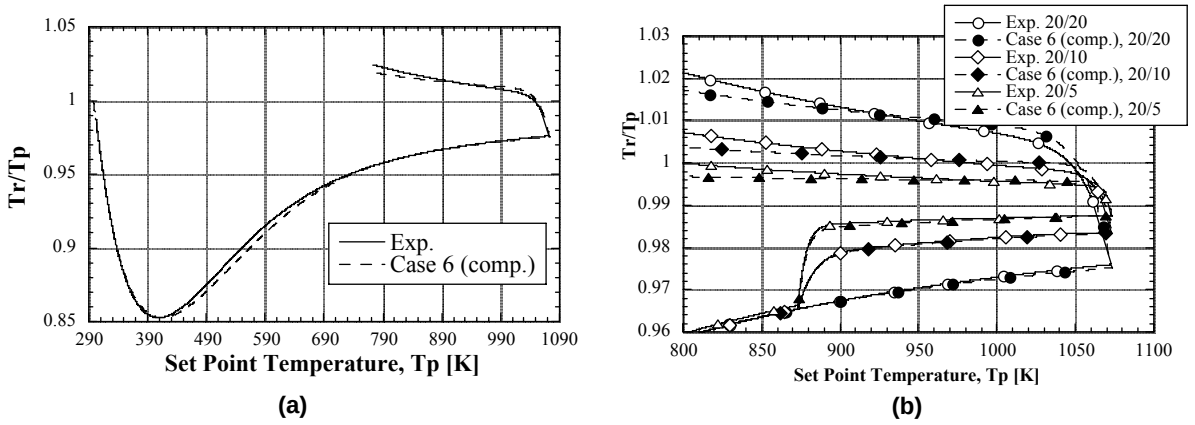

Figure 4.4. Ratio between the reference plate temperature and set point temperature for case 6 (Table 4.3): (*a*) constant heating and cooling rate; (*b*) variable heating and cooling rates of empty pan (case 6).

This excellent agreement at multiple heating rates validated the proposed model. Immediately after the heating/cooling transition, the computed ratios T_r/T_p were larger than the experimental ones and followed quite well the experimental results upon cooling. Upon cooling, the slope of the T_r/T_p curve was smaller than those corresponding to experimental results.

The next step in the analysis of the DSC signal was to investigate model parameters relevant to the phase transition. DSC experiments were conducted for a pure aluminum sample (mass 0.01714 g). A sapphire reference material of 0.04212 g was placed in the reference container. A small phase change effect was seen on the reference side (Figure 4.5). When the radiation between the two containers was not included, the computed T_r/T_p increased at the same rate as that before the phase change. The characteristic behavior of T_r/T_p during the phase change was accurately reproduced when (*a*) $\tau_{C1} = 3.3$ s and the radiative exchange was included between the two containers, or (*b*) $\tau_{C1} = 0.33$ s and the radiation exchange was excluded between the two containers.

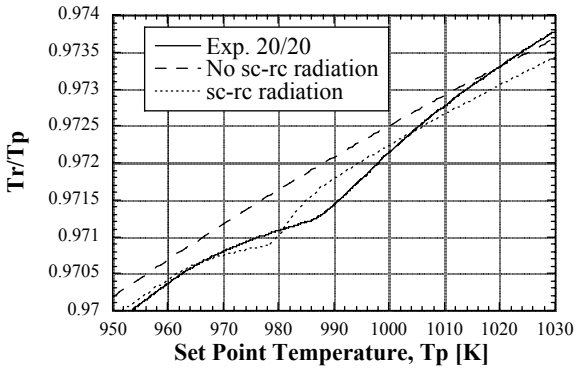

Figure 4.5. T_r/T_p results for temperature lag on the reference side for a pure aluminum sample (cases 6 and 7, Table 4.3).

For $T_s - T_r$, experimental results were compared against numerical simulation results for empty containers [Figure 4.6(a)]. The computed values were lower for heating and higher for cooling than the experimental data. This result indicated that conduction and radiation parameters alone cannot account for the asymmetry seen in the experiments; therefore, an asymmetry submodel had to be developed. Experiments were conducted for pure aluminum.

Numerical simulations were performed for case 6 by including the sample and the reference in the analysis. Figure 4.6(*b*) shows the results for the temperature difference $T_s - T_r$. The abrupt variations in the values for $T_s - T_r$, which were due to the phase transformations, were qualitatively reproduced by the proposed model. The computed values for $T_s - T_r$ were lower at heating and higher at cooling than the experimental data. The results at that time, using an intermediate model as shown in Figure 4.6, demonstrated that the intermediate model was not able to describe the asymmetry phenomena for the instrument.

4.1.4 Results for Differential Temperature

Ideally, the instrument signal should show a zero baseline when no samples are used. The instrument showed that, after an initial decrease, the dV signal increased with temperature. The same overall curve variation was observed when no pans were used and when platinum pans were used (Figure 4.7). This fact indicated that there were some intrinsic differences between the sample side and the reference side that caused a signal difference between the two sides of the instrument. This effect is now referred to as instrument asymmetry.

Experiments indicated that the initial drop was due to (*a*) the mass difference between the sample side and reference side and (*b*) different time constants for the thermocouple assemblies on the sample and reference sides. Changing the position of the sensing unit inside the furnace decreased the systematic error, but it could not be removed. Moreover, the temperature distribution of the furnace walls and the temperature distribution within the DSC instrument were nonuniform such that the sample and the

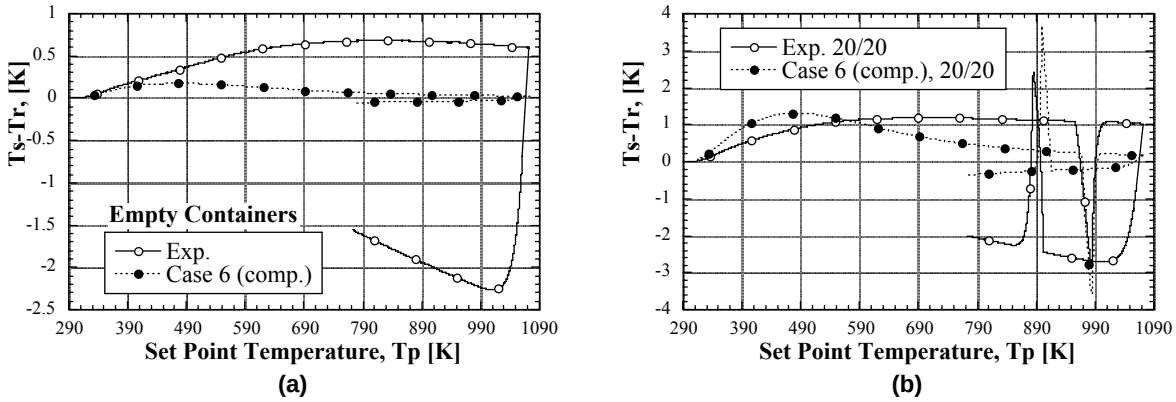

Figure 4.6. Temperature difference between the sample plate and reference plate for (*a*) empty containers and (*b*) a pure aluminum sample.

reference plates were not exposed to an equivalent temperature environment. These geometric effects could be considered the result of simple conduction and radiation mechanisms between the instrument parts. These geometric asymmetries were modeled based on the actual curve variation of the systematic error.

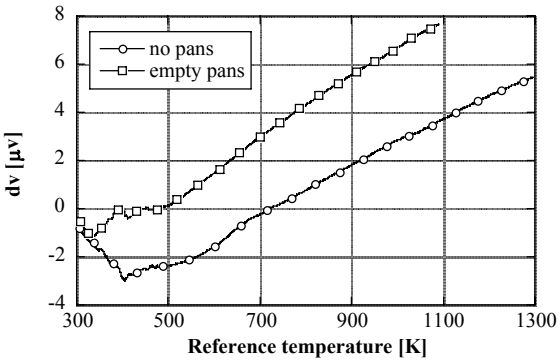

Figure 4.7. Signal difference between sample side and reference sides for no pan and empty pan cases showing a systematic instrument error.

The instrument asymmetry was shown to be dependent on temperature and the heating/cooling rate. Also, the variation of instrument asymmetry during changes in the heating/cooling rate showed typical lags that were described using time-constant equations. We tried various formulations to take the instrument asymmetry into consideration. Because the asymmetry was present for runs when no containers were used, the asymmetry was then modeled as a source term in the sample plate equation. This source-term formulation did not adequately describe the heating-rate dependence. In order to account for the asymmetry, the following model was adopted for the temperature difference between the sample side and the reference side, $T_s - T_r$:

$$\begin{aligned} T_S - T_R &= T_2 - T_1 + \varepsilon_A \\ \frac{d\varepsilon_A}{dt} &= \frac{\varphi - \varepsilon_A}{\tau_A} \\ \varphi(y_0, \alpha) &= (y_0 - 1)(g_1\,\alpha - g_0) \end{aligned} \qquad (4.1.1)$$

where ε_A is the asymmetry term. In order to account for the rate dependence, the evolution of the asymmetry term was described by a time constant–like equation. The term τ_A is a time constant whose values would be similar in value to the furnace time constant, $\tau_{CF.}$ The term α was the heating rate, while g_1 and g_0 were constant parameters. The following parameters were found to give the best agreement for $T_s - T_r$: τ_A = 40s, g_0 = 0.0011, and g_1 = 2.22 (s).

The computational results were compared with experimental data for baseline runs (i.e., runs using empty containers) and runs using pure aluminum. The cases considered are identified in Table 4.4. The experimental and computational results were used to identify the most critical model features in order to reproduce all the typical features of a DSC signal. Initially, experiments were performed at heating rates of 20°C/min from room temperature until the set point reached a temperature of 1073 K, followed by cooling at a rate of 20°C/min. The same model parameters were considered for each case. The representative parameters for each case are shown in Table 4.5. Sabau et al. [17] showed that for this model there was a good fit for the reference temperature results. However, the results for the temperature difference $T_s - T_r$ between the sample plate and the reference plate showed poor agreement because instrument asymmetry was not considered.

In this section, only results for $T_s - T_r$ are presented. Figure 4.8(a) shows $T_s - T_r$ for the temperature range common to all cases considered. There was good agreement with experimental results for baseline runs. For sample runs, computational results showed larger values at low temperatures. At higher temperatures, there was good agreement with experimental results for baseline runs as well as for sample runs for all cases considered [Figures 4.8(b) and 4.9(a,b)]. However, the position of the computed peaks at cooling, which were due to a phase change, were observed at higher temperatures than those observed experimentally. These results provided experimental validation of the proposed asymmetry formulation, since the $T_s - T_r$ data were reproduced during the transition to different heating rates and cooling rates.

Table 4.4. Cases considered for numerical simulations

Case ID[a]	Heating rate	Temperature / time at heating rate change	Heating rate	Temperature / time at heating-cooling transition	Cooling rate
B1	20	—	20	800 / 2324.7	20
S1	20	—	20	800 / 2324.7	20
B2	20	600 / 1724.7	10	800 / 2924.7	10
S2	20	600 / 1724.7	10	800 / 4124.7	10
B3	20	600 / 1724.7	5	800 / 4124.7	5
S3	20	600 / 1724.7	5	800 / 4124.7	5

[a] B = baseline case; S = sample case.

Note: Temperatures in °C, time units in seconds, and rates in °C/min.

Table 4.5. Time constants (in seconds) for cases considered for numerical simulations ($\tau_{C1} = \tau_{C2} = 3.3$, $\tau_{C3} = \tau_{C4} = 0.01$, $\tau_{C5} = 1$, $\tau_{C6} = 10$ s)

Radiation parameters							Furnace	Stem parameters	
τ_{R1}	τ_{R2}	τ_{R3}	τ_{R4}	τ_{R5}	τ_{R6}	τ_{R8}	τ_{CF}	τ_{C7}	τ_{R7}
650	1000	680	220	200	6300	4000	30	2500	30000

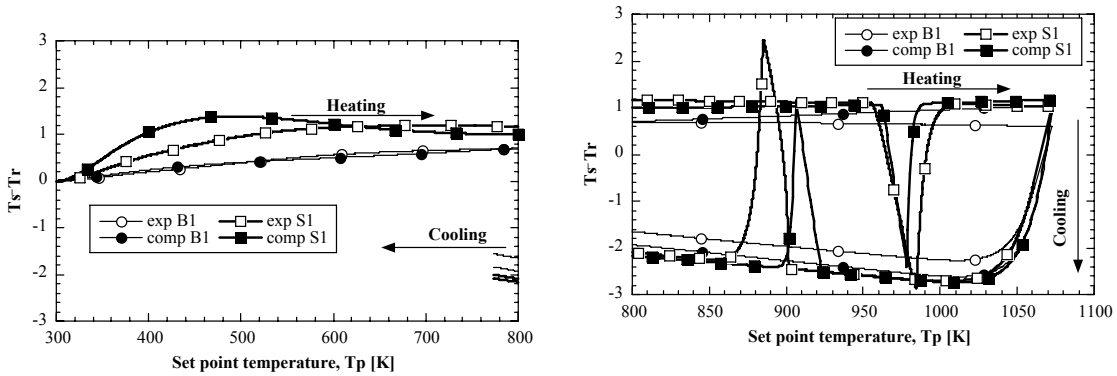

(a) (b)

Figure 4.8. Temperature difference between the sample plate and reference plate for cases B1 and S1 for temperature domains of (*a*) [300:800] K and (*b*) [800:1100] K.

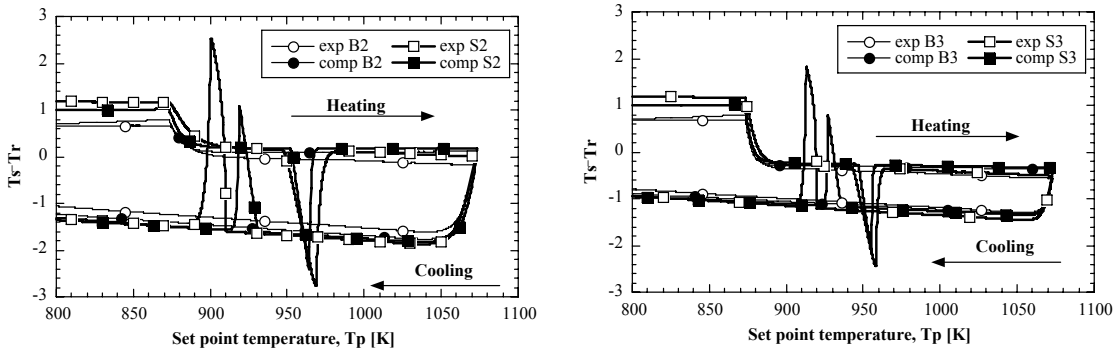

(a) (b)

Figure 4.9. Temperature difference between the sample plate and reference plate for the high-temperature domain [800:1100] K: (*a*) cases B2 and S2 and (*b*) cases B3 and S3.

4.1.5 Results for Solid Fraction Distribution

In the approach described in the previous sections, numerous parameters were required for the determination of the solid fraction distribution. Some of these physical parameters were obtained from calibration experiments, while others were obtained from an inverse analysis of parameter-estimation type. Traditional inverse methods were applied to the DSC model [18,19]. This project pioneered the application of inverse analysis to DSC data. We found, however, that traditional inverse methods yielded limited success with the DSC system.

Instead, we developed an alternative direct approach to the inverse method that enabled determination of the enthalpy and ensuing distribution of the solid fraction during solidification. This direct approach proved to be a reliable and efficient technique for analyzing the DSC data. Model

parameters were also obtained for the melting of pure aluminum. Pure aluminum melts at a single well-known temperature. Based on several simulations, an appropriate combination of model parameters were determined such that (*a*) the enthalpy change occurred over a minimum temperature range, and (*b*) the latent heat of solidification was approximately the same as that determined experimentally. The data obtained for enthalpy are shown in Figure 4.10.

Once an optimum combination of model parameters was determined for pure aluminum, simulations were carried out for a commercial aluminum alloy, A356. The data obtained for the fractional latent heat release during melting and solidification are shown in Figure 4.11. The data for the solid fraction were obtained by simple integration of the raw DSC data. As shown in the figure, the thermal lag between the two distributions of the solid fraction, which were obtained at heating and cooling, was drastically reduced. The computed distribution for the solid fraction was deemed consistent with that obtained by other studies.

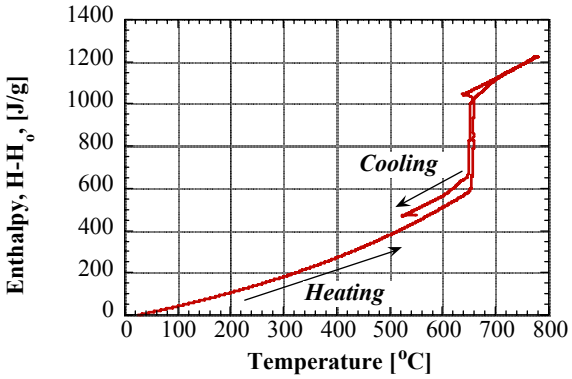

Figure 4.10. An alternative approach to inverse analysis accurately predicted the enthalpy of pure aluminum. The computed value for the latent heat at heating and cooling was 429 and 382 J/g, respectively, for an average of 405 J/g, while the experimentally measured value was 397 J/g.

With the final direct DSC model, there was an incompatibility between the accuracy of enthalpy values and latent heat distribution. The following trends were observed: (*a*) larger enthalpy values than those expected were obtained when accurate distributions of the latent heat were obtained; and (*b*) the latent heat distribution exhibited low accuracy when enthalpy values were accurately predicted. Thus, the user should focus on calibrating the model not for the average enthalpy but for its evolution as a function of temperature during phase changes.

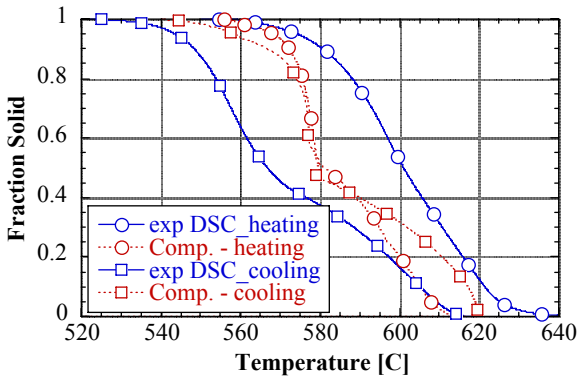

Figure 4.11. The computed fraction solid for alloy A356 using the current DSC model. Solid lines indicate data for the solid fraction; dotted lines, data for current DSC model.

4.1.6 Industrial Interaction: Application to Investment Casting Program

As an additional opportunity to validate the results of the modeling and improved experimental procedures determined from this project, the computational approach was utilized in another project, "Predicting Pattern Tooling and Casting Dimensions for Investment Casting" (DE-FC36-01ID14003), in order to obtain optimal thermophysical properties for aluminum alloy 356.[1] The use of the fractional latent heat distribution was then used for the numerical simulation of the investment casting

[1] The participants in the Investment Casting project were Schrey & Sons Mold, Buycastings.com, Precision Metalsmiths Inc, J&J, A. DePuy Co., Precision Colloids, Precision Metalsmiths Inc., Minco Inc., JEM Mfg., S&A Consulting Group, Argueso & Co., Precision Castings Inc., and EMTEC.

process. The data obtained with the DSC model were important for the timely completion of the tasks associated with the heat transfer phenomena.

The solid fraction data provided accurate information on the solidification path for alloy 356 (Figure 4.12). Without this data, advances in the investment casting project would have been limited. This application to the investment casting project demonstrated that the current work on the DSC model could be directly applied to commercial alloys, thus illustrating an immediate benefit to the metal casting industry.

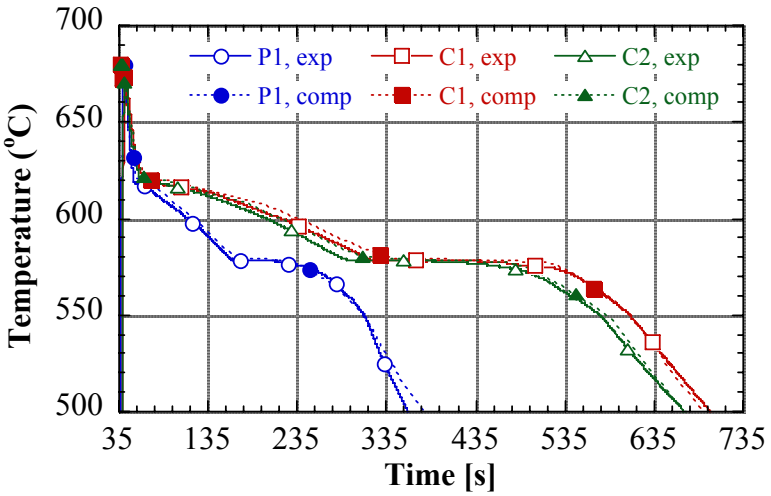

Figure 4.12. Comparison between thermocouple data and predicted model temperatures at three locations, showing excellent agreement for an investment casting.

4.2 Dual Push-Rod Dilatometer

Dilatometry involves deducing volume changes as a function of sample temperature. Owing to inherent thermal lags in a system setup, careful analysis is required to estimate the sample temperature based on remote thermocouple readings. One of the main barriers in the analysis of materials processing and industrial applications is the lack of accurate experimental data on material thermophysical properties. To date, the measurement of most high-temperature thermophysical properties is often plagued by apparent temperature lags. These temperature lags are inherent to the measurement arrangement since (*a*) the sample temperature cannot be directly measured and temperature data are recorded by using a thermocouple that is placed at a location other than that of the sample, and (*b*) there is a nonhomogeneous temperature distribution within the instrument [5,8].

A schematic of the original dilatometer system for molten density measurements is shown in Figure 4.13(a). This configuration, which is not geometrically optimal owing to the remote location of the single thermocouple, produces a substantial thermal lag in dynamic studies between the actual sample and thermocouple temperatures. Inferring the proper sample temperature from such a configuration requires a complicated mathematical model. Figure 4.13(b) displays a schematic of the modified sample assembly. This symmetric assembly permits lumped heat transfer models for both the sample holder and sample. Figure 4.14 shows photographs of the old and new sample configurations.

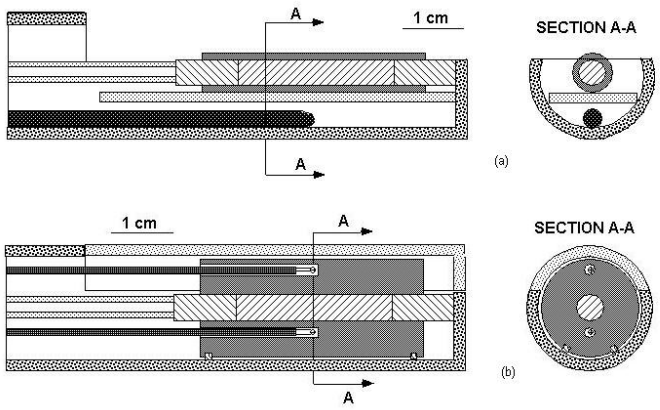

Figure 4.13. Schematics showing (*a*) the original dilatometer setup and (*b*) the modified dilatometer.

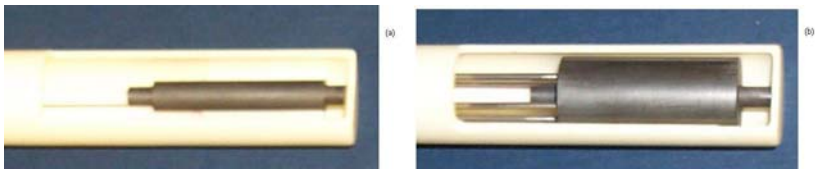

Figure 4.14. Photographs showing (*a*) the original dilatometer sample region and (*b*) the modified dilatometer sample region with sample holder.

Figure 4.15 presents the geometric description used in the heat transfer analysis. If a temperature gradient exists between the radially placed thermocouples, then an inverse heat conduction analysis [20–22] is required for estimating the surface heat flux penetrating the sample. A well-designed experiment removes the need for a complicated inverse analysis. It should be noted that several inverse heat conduction codes based on the method of Frankel and Keyhani [23], Green's functions [24], and space marching [25] were prepared and tested for this project. However, owing to the highly ill-posed nature of inverse heat conduction, data processing [26] is required in order to arrive at a high-quality surface heat flux prediction. The choice of graphite [27] removed the need for a spatial solution in the sample holder because of the large thermal conductivity of this material and the heating rate ranges used in practice.

This section of the report describes the sample holder modification used in the existing dilatometer (Sect. 4.2.1), an analytic heat transfer model for the sample based on using the sample-holder temperature measurements (Sect. 4.2.2), and preliminary numerical findings correlating the sample density to the inferred sample temperature for a common aluminum alloy in the phase-change regime (Sect. 4.2.3).

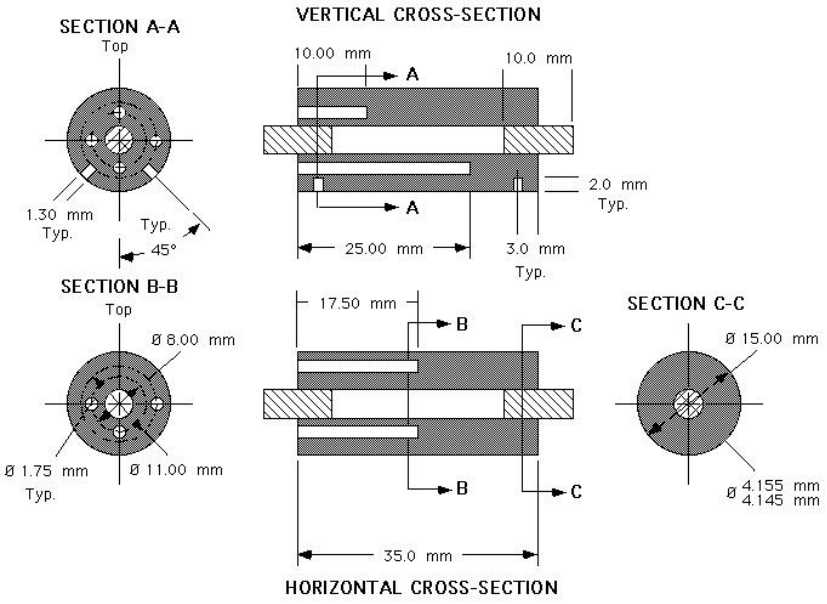

Figure 4.15. Schematic of geometry showing thermocouple placements.

4.2.1 Experimental Procedure, Data Processing, and Assumptions

This section presents an overview of the entire experimental procedure used in the acquisition of the necessary data for the model developed in Section 4.2.3.

Experimental Procedure

The dilatometer used in the present study was a Theta Industries dual push-rod horizontal dilatometer. For the purposes of this work the dilatometer was set up in the single-rod configuration. The sample holder tube and the push-rod were constructed of high-purity alumina. The push-rod was attached to a linear variable differential transducer (LVDT) used for displacement measurements. The LVDT was leafspring-mounted and housed in a temperature-controlled enclosure that also served as the location of the cold junction for all of the thermocouples used for specimen temperature measurements. The LVDT displacement calibration factor was determined through the use of a precision micrometer and gauge blocks. The aluminum alloy used for the study was a ternary analogue of the commercial aluminum-silicon casting alloy, A356. The composition of the ternary alloy was Al–6.92 Si–0.42 Mg wt % and was chosen to match the composition used in calculations of the solid fraction using the diffusion simulation software DICTRA^{TM}. The container developed to hold the molten specimen was a thick-walled graphite cylinder with graphite end plugs. The cylinder bore and outer diameter (OD) of the plugs were precision-ground and matched as a set to ensure a near air-tight seal while still allowing for the free movement of the end plugs required to accurately follow the changes in length of the specimen. The material used for the specimen holder and end plugs was fine-grained isotropic POCO AXF-5Q graphite, whose expansion behavior had been characterized previously. The specimen holder OD was slightly less than the sample holder tube inner diameter (ID) and was isolated from the holder tube by four small-diameter alumina pins acting as supports.

The dilatometer system correction factor, which must be determined for single push-rod systems, was determined by comparing the experimentally measured values for the expansion of a National Institute of Standards and Technology (NIST) standard reference material (SRM) 737 tungsten rod

with the certified expansion values of the SRM. This correction run was made with the two graphite plugs from the specimen holder located on each end of the tungsten rod, as they would be during the alloy melting run, and used the same temperature schedule. The thermocouples used for the study were Type K, special grade, and were metal sheathed with closed ungrounded ends. Special precautions were taken to minimize thermally generated electromagnetic fields at connections in the thermocouple circuits. The temperature schedule used for the alloy melting run was 20°C/min to 450°C, followed by a 30-min isothermal hold. The heating rate then changed to 1°C min, and heating was continued to a maximum setpoint of 800°C . The specimen was cooled through the solidification range at a rate of 1°C /min. Data was recorded in the melting range of the alloy specimen at a rate of one reading every 6 s. Prior to testing, the dilatometer was evacuated to 100 μm using a mechanical vacuum pump and backfilled with titanium-gettered high-purity helium. This procedure was repeated three times before heating was started. A helium flowrate of 5 sccm was used during the dilatometer runs.

Data Processing

Processing of the dilatometer data required several steps. The raw LVDT position data (volts) must have the system correction values determined in the tungsten SRM run added to them. Next, the initial value of the LVDT must be subtracted from the data to result in a change in position and the LVDT calibration factor applied to give the change in specimen length (mm). Up to the solidus temperature, this delta length is used to calculate the expansion of the specimen and the specimen length and diameter at any temperature. Above the solidus temperature, the graphite expansion is used to calculate the specimen container ID and the specimen diameter. In this region the specimen length is still calculated from the corrected and adjusted LVDT data. Finally, the density as a function of temperature is calculated by dividing the initial specimen mass by the calculated specimen volume.

Assumptions

The calculation of density from specimen length changes determined by dilatometry requires assumptions to be made. The first assumption that must be made is that the mass of the specimen does not change during the measurement. This assumption can be validated with a check of the specimen weight after the dilatometer run and a visual inspection to ensure that no molten material extruded past the end plugs. The second assumption is that the diameter of the specimen is uniform and known at all temperatures. Up to the solidus temperature of the alloy, the diameter of the specimen can be calculated by applying the expansion of the alloy at a given temperature to the initial diameter. Above the solidus temperature, it must be assumed that the specimen is a fluid that takes on the shape of its container. In this region the specimen diameter is assumed to be that of the inner diameter of the graphite specimen holder, which also can be calculated from the known expansion of the graphite and the initial holder ID. This assumption is aided by the fact that the push-rod is spring-loaded against the end plugs and both end plugs are free to move. During the initial region of melting of an alloy, there may be a short temperature interval where the specimen has a network of solid material remaining and has not completely filled the container. The assumption of known sample diameter is not valid in this region, and the density cannot be calculated for this temperature interval.

4.2.2 Mathematical Model

ORNL has redesigned the dilatometer sample holder in order to ensure the uniform heating of the test sample under consideration. This concept, used in conjunction with mathematical modeling, permits the accurate extraction of and correlation between both the sample density and predicted sample temperature. The redesigned ORNL dilatometer sample holder renders a nearly isothermal region.

Four embedded thermocouples, as shown in Figure 4.15, are used to indicate that the container is isothermal at any instant in the experimental process. This observation is attributed to the high thermal conductivity of the shell. Additionally, the thermal mass of the sample holder is much greater than the thermal mass of the sample. Thus, at any instant of time only one temperature value is actually required. Simultaneously, the LVDT permits the changes in the length of the specimen to be recorded.

Preliminary Analytic Assumptions

We made several simplifying assumptions. The assumptions permitted a relatively simple but robust model to be developed. Concerning measurement, the following considerations can be made:

(a) The initial mass of the specimen, m, and its geometry are known at room temperature.

(b) Thermal expansion is accounted for in the graphite sample holder [15], end plugs, and sample.

(c) The sample volume follows $V(t) = V_o(1 + \Delta s/s_o)^3$ in the premelt stages and is assumed to retain its cylindrical shape in the melt phase, where $r_a(t)$ is the sample radius, and $\Delta s = s(t) - s_o > 0$, where $s(t)$ is the sample length and s_o is the initial sample length at room temperature. The sample is carefully sized such that at the onset of melting, ideally speaking, the sample radius attains the value of the sample holder, i.e., $r(t) = r_a(t)$. At times, this assumption is not valid [i.e., $r(t) \neq r_a(t)$ and $r_a(t)$ must be estimated; therefore, $V(t) = \pi r^2_a(t)\, s(t)$, $s(t) > s_o > 0$].

(d) The sample length changes are obtained by adjusting the LVDT data with the corresponding thermal expansion of the graphite holder, graphite plugs, and alumina rod.

(e) The mass of the specimen does not change with time, implying $dm = 0 = d(\rho(t)\, V(t))$, where $V(t)$ is the sample volume. Note that $\rho(t)$ is considered to be known from the dilatometer but requires correlation to the sample temperature, $T_s(t)$.

(f) The heat capacity, $c(T_s)$, latent heat, H, and solid fraction $f_s(T_s)$ of the sample are known.

(g) The output behavior of the LVDT for the push-rod dilatometer is usable for identifying the times when the sample reaches its solidus and liquidus temperatures.

(h) The liquidus and solidus temperatures for the sample are known.

(i) The furnace assembly uses helium at 1 atm.

Melt-Regime Modeling

The focus of the present study lies in the melt regime of aluminum alloy A356. Therefore, this section presents only the developments pertinent to this heat transfer regime. The melt regime is defined with the aid of two distinct times, namely, $t = \tau_1$ and $t = \tau_2$. Here, τ_1 is the time when the sample attains its solidus temperature ($T_s(\tau_1) = T_{\text{sol}}$, $f_s(T_s(\tau_1)) = 1$) while τ_2 is the time when the sample attains its liquidus temperature ($T_s(\tau_2) = T_{\text{liq}}$, $f_s(T_s(\tau_2)) = 0$). Key to this study is the ability to identify these times based on the LVDT output.

The overall heat equation for the sample in the phase-change regime is given by

$$-\rho(t)H\frac{df_s(T_s)}{dt}+\rho(t)c(T_s(t))\frac{dT_s(t)}{dt}=-2\frac{h(T_s,T)}{r_a(t)}(T_s(t)-T(t)),\ \tau_1\le t\le\tau_2, \tag{4.2}$$

where $f_s(T_s)$ ε [1,0] is the solid fraction, and $h(T_s,T)$ is the unknown heat transfer coefficient defined between the sample and sample holder. Note that end effects are neglected owing to the sample geometry. It is evident from Eq. (4.2) that both $T_s(t)$ and $h(T_s,T)$ are presently unknown. This dilemma can be resolved by introducing a physical constraint that is available from the experiment. That is, if one can identify the time at which the sample reaches the liquidus temperature, then a second independent expression is generated to close the system and eliminate the heat transfer coefficient. The LVDT output stream possesses this information.

The behavior of the solid fraction, $f_s(T_s(t))$, is assumed to be known in either tabular or functional form. The solid fraction time derivative can be expressed in two components using the chain rule of differential calculus [28], namely,

$$\frac{df_s}{dt}=\frac{df_s}{dT_s}\frac{dT_s}{dt}, \tag{4.3}$$

where df_s/dT_s is a known property. Equation (4.2) can now be expressed as

$$\rho(t)\frac{dT_s(t)}{dt}(c(T_s(t)-H\frac{df_s(T_s)}{dT_s})=-2\frac{h(T_s,T)}{r_a(t)}(T_s(t)-T(t)),\ \tau_1\le t\le\tau_2, \tag{4.4}$$

subject to $T_s(\tau_1)=T_{sol}$ or

$$\frac{dT_s(t)}{dt}=-\frac{2\frac{h(T_s,T)}{r_a(t)}(T_s(t)-T(t))}{\rho(t)(c(T_s(t)-H\frac{df_s(T_s)}{dT_s})}\ ,\ \tau_1\le t\le\tau_2, \tag{4.5}$$

Integration of Eq. (4.5) into the melt domain yields

$$T_s(t)=T_s(\tau_1)-2\int_{u=\tau_1}^{t}\frac{\frac{h(T_s,T)}{r_a(u)}(T_s(u)-T(u))}{\rho(u)(c(T_s(u)-H\frac{df_s(T_s)}{dT_s})}du\ \ ,\ \tau_1\le t\le\tau_2, \tag{4.6}$$

where u is a dummy variable of integration. Evaluating Eq. (4.7) at $t=\tau_2$ yields

$$T_s(\tau_2)=T_{liq}=T_{sol}-2\int_{u=\tau_1}^{\tau_2}\frac{\frac{h(T_s,T)}{r_a(u)}(T_s(u)-T(u))}{\rho(u)(c(T_s(u)-H\frac{df_s(T_s)}{dT_s})}du\ \ , \tag{4.7}$$

where the liquidus temperature T_{liq} is known. Using the weighted mean-value theorem [28], the average heat transfer coefficient, h_m, valid in the melt domain, is given as

$$h_m = \frac{T_{sol} - T_{liq}}{2\int_{u=\tau_1}^{\tau_2} \frac{T_s(u) - T(u)}{r_a(u)\rho(u)[c(T_s(u)) - H\frac{df_s}{dT_s}]}du}, \quad \tau_1 \le \tau \le \tau_2 . \tag{4.8}$$

The reduced heat equation, defined by replacing $h(T_s,T)$ with h_m in Eq. (4.4), becomes

$$\frac{dT_s(t)}{dt} = -\frac{2h_m(T_s(t) - T(t))}{r_a(t)\rho(t)(c(T_s(t) - H\frac{df_s(T_s)}{dT_s})}, \quad \tau_1 \le t \le \tau_2, \tag{4.9}$$

subject to $T_s(\ _1) = T_{sol}$. Equation (4.9) has explicitly removed the need for knowing the heat transfer coefficient in lieu of introducing a physical constraint. A simple, iterative numerical procedure is implemented for determining the sample temperature $T_s(t)$. Once $T_s(t)$ is known, then the average heat transfer coefficient, h_m, can be numerically determined from Eq. (4.8).

For numerical convenience, the required property df_s/dT_s is now expressed in an analytic form based on a limited data set. It is possible to form a global approximation or interpolant for the function $f_s(T_s)$ using the N-term truncated series [29]

$$f_s(T_s) = \sum_{j=1}^{N} a_j \sqrt{\beta^2 + (T_s(t) - T_{s,j})^2}, \tag{4.10}$$

where β is the shape factor and $\{T_{s,j}\}_{j=1}^{N}$ represents the interpolant centers. This procedure requires the determination of the expansion coefficients a_j, $j = 1, 2, \ldots, N$ from the set of data for $f_s(T_{s,j})$ at measured $T_{s,j}$ $j = 1, 2, \ldots, N$. With this, the required property df_s/dT_s necessary for Eq. (4.3) is easily calculated by analytic differentiation.

Determining the Time Domain for Phase Changes

A typical LVDT sample length output over time (corrected and adjusted as previously described) is displayed in Figure 4.16. Data are shown prior to and past the melt regime. This sample length output plot is used to estimate τ_1 and τ_2 for the results displayed in the next subsection. The solid red line segments are tangents drawn indicating a nonmelt regime. The departure points can be used to locate the values of τ_1 and τ_2. The point of detachment from the lower line segment from the data estimates τ_1, while the point of detachment from the upper line segment from the data estimates τ_2. As a physical check, the value of τ_1 should be greater than that of the time when the embedded thermocouple in the sample holder reads the value of the solidus temperature, T_{sol}. Additionally, apriori knowledge of the sample liquidus temperature should be used to physically check the value of τ_2. This time value should be greater than the time at which the sample-holder thermocouple reads the liquidus value, T_{liq}. Figure 4.16 data are used for the results presented in Section 4.2.3, where the heating rate is 1°C/min. in the melt domain.

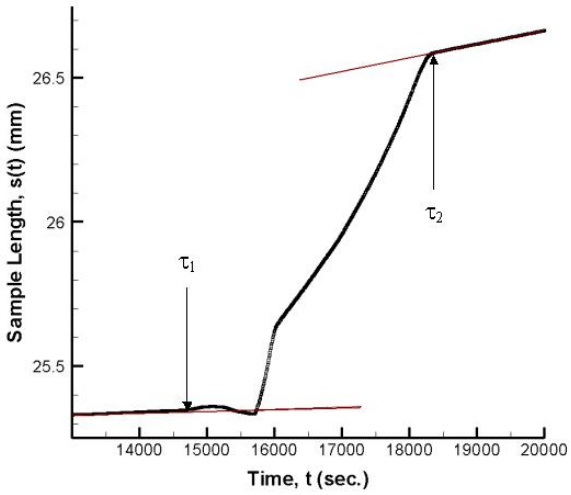

Figure. 4.16. Typical sample length output used to estimate τ_1 and τ_2 (programmed heating rate is 1°C/min.).

4.2.3 Results

The focus of this research lay in developing an accurate correlation between the sample density and sample temperature for alloys in the melt regime based on remote temperature measurements. Figure 4.17 presents the solid-fraction data and the constructed radial basis function (RBF) global interpolant over the sample temperature for A356. Twelve solid-fraction data points are identifiable at the locations of rapid changes in the slope. The resulting RBF approximation described in Eq. (4.10) uses $\beta^2 = 0.05$ and an equidistant distribution of centers. It is interesting to note that piecewise linear interpolation between the data points is graphically identical to the present solid line. However, numerical differentiation of piecewise continuous functions requires special care at the nodes. Additionally, it should be observed that Eq. (4.10) is infinitely differentiable for $\beta^2 \neq 0$. Figure 4.17 also presents, on the second y-axis, df_s/dT_s. For A356, an eutectic behavior is observable near 570°C, and thus a large value for df_s/dT_s is expected.

The thermophysical parameters for A356 used in this preliminary investigation are taken as H = 429 J/g [22], $c(T_s) = c$ = 1.19 kJ/(kgK) [30], and the sample mass is measured as 0.87709 g. The initial geometric length of the specimen, s_o , is 25.001 mm, while the sample diameter and ID of the holder are 4.107 mm and 4.145 mm, respectively. The solidus and liquidus temperatures are 551°C and 614°C, respectively. The total number of temporal data points used in the region defined by τ_1 = 14650 s and τ_2 = 18359 s is 582 points. It is presently assumed that $r_a(t) = r(t)$. The preliminary test case uses a heating rate of 1°C /min from $t \neq 8{,}000$ s to $t \approx 28{,}000$ s. The sample was maintained at an isothermal hold prior to experiencing this heating rate in order to ensure system equilibrium. With the collected sample-holder temperature data, the numerical procedure was implemented for estimating the sample temperature based on Eq. (4.9). The iterative numerical procedure required 23 iterations

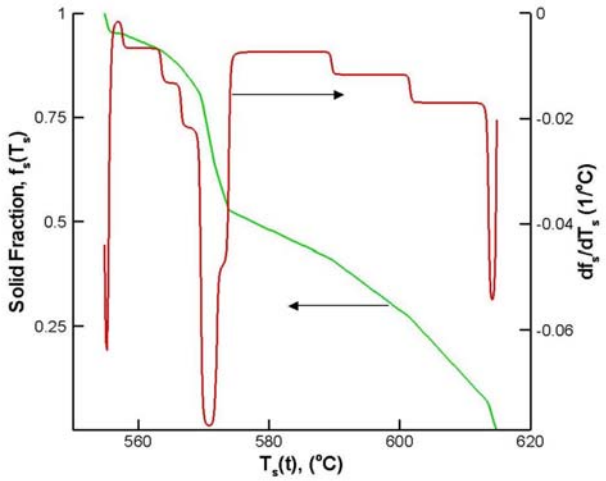

Figure 4.17. Solid fraction, df_s/dT_s and its sample temperature derivative, df_s/dT_s as a function of sample temperature when $\beta^2 = 0.05$ for A356.

using a conventional, forward Euler method with a relaxation constant of 0.5. Trapezoidal rule integration was used for calculating h_m. It was determined that $h_m = 1.99$ kW/(m^2 °C). This value for the average heat transfer coefficient lies within the estimated bandwidth given in Ref. 31 (p. 90, Figure 5.13, at the onset of the experiment, which corresponds to a similar physical problem and material as proposed here).

Figure 4.18 shows the sample length, $s(t)$, and thermocouple temperature data, $T(t)$, in the melt domain time span given by $t \in [\tau_1,\tau_2]$. The LVDT voltage has been carefully converted to displacement in this figure. Figure 4.19 presents the density, $\rho(T_s)$, as a function of the numerically calculated sample temperature using the proposed numerical procedure. This figure also presents the solid fraction in order for the reader to clarify the density behavior in the vicinity of the eutectic temperature (570°C). Figure 4.20 presents the sample holder temperature, $T(t)$, and sample temperature, $T_s(t)$, over the melt time domain. The eutectic behavior of a material affects the sample temperature upon external heating. The embedded thermocouple temperature readings continue to rise as energy is continuously deposited into the system from the heater. However, the sample temperature, upon encountering an eutectic region, tends to remain relatively flat [see Eq. (4.9) as $df_s/dT_s \rightarrow \infty$]. For this example, the analysis adjusts the sample temperature by approximately 0.75°C as indicated by the second y-axis detailing the temperature difference between the sample and the holder, $T(t) - T_s(t)$, over the time span of interest.

Finally, Figure 4.21 presents a comparison of sample density results over sample temperature between the original configuration displayed in Figure 4.13(a) and the new sample holder configuration shown in Figure 4.13(b). Figure 4.21 illustrates that a substantial correction is achieved through the combination of sample holder design and inverse analysis. For example, the density of 2.5 g/cm^3 is now estimated to be achieved at 582°C, whereas previous results would have correlated this density to 591°C. This is a substantial difference.

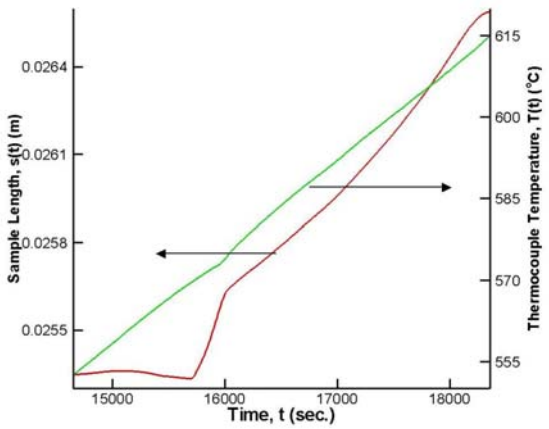

Figure 4.18. Sample length, *s(t)*, and thermocouple temperature, *T(t)*, against measured time *t* in melt regime.

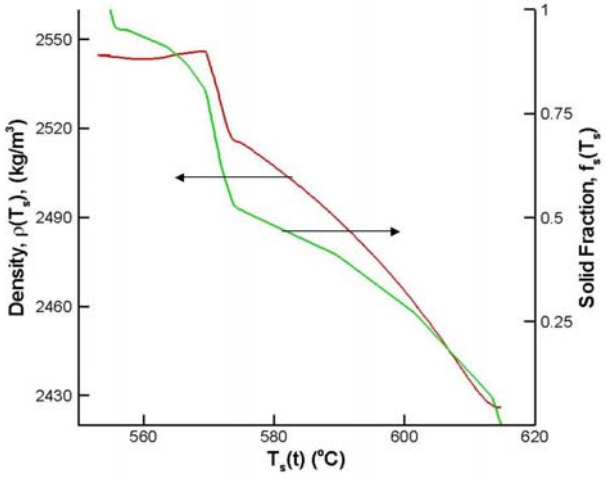

Figure 4.19. Desired density, $\rho(T_s(t))$, and solid fraction, $f_s(T_s(t))$, as a function of predicted sample temperature, $T_s(t)$.

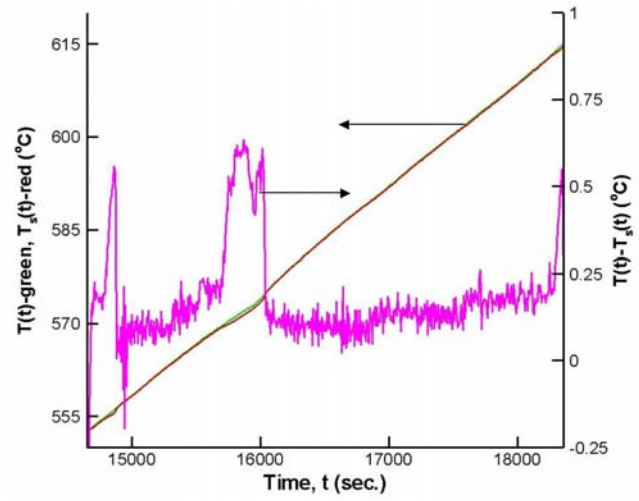

Figure 4.20. Comparison between thermocouple temperature, *T(t)*, and predicted sample temperature, $T_s(t)$, over time *t*.

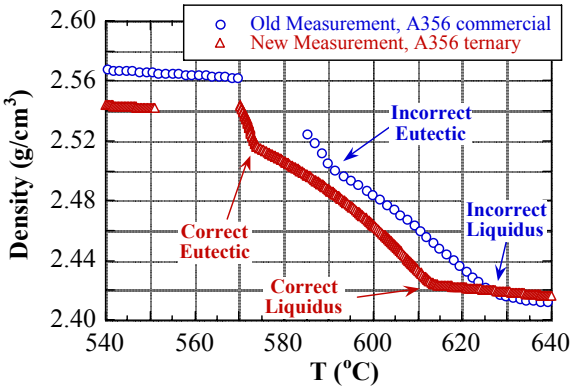

Figure 4.21. Comparison between old and new sample holder sample density predictions.

4.2.4 Summary

The experimental results reveal that it is possible to accurately infer the sample temperature based on sample-holder temperature measurements using the newly proposed modified holder assembly. This inference is obtained through the careful orchestration of experimental design and analysis. The new configuration minimizes geometrically induced lags and accounts for the phase-change-induced lag through a mathematical model, as measured from a distant thermocouple in the sample holder. The results presented here offer insight into developing a dilatometer holder assembly that permits the characterization of high-temperature alloys in the melt regime. Sample density measurements can now be correctly correlated with an estimated sample temperature that accounts for thermal lags

inherent to the dilatometer design. Further refinements in the model could involve (*a*) experimentally determining the sample latent heat, H, and the specific heat, c_p, and (*b*) refining the solid fraction curve to include additional data points and thereby obtain a smoother representation of its derivative with respect to temperature.

5. Accomplishments

For convenience, a web site containing pertinent papers, reports and other information on this project has been established at http://www.ms.ornl.gov/mpg/sabau.htm.

5.1 DSC

In order to describe the DSC system with minimal components, an analysis was performed to ascertain the effect of each of the components. An alternative direct approach to the inverse method was developed in order to determine the enthalpy and ensuing distribution of the solid fraction during solidification. This direct approach proved to be very reliable and an efficient technique for performing and analyzing DSC data. The DSC heat transfer model was validated for pure aluminum and successfully applied to a study of the commercial aluminum alloy A356. Prior to this R&D, DSC systems yielded an estimated error for the solid fraction of approximately 30%. As a result of this project, dilatometer temperature error has been reduced to approximately 6°C at temperatures of 600-700°C. This project has led to very accurate solid fraction data measurements with 3% error and reduced the temperature error for improved density measurements to 0.5°C.

5.2 Dilatometer

The contribution of this portion of the project involved (*a*) the design, fabrication, instrumentation, calibration and testing of a new sample holder for an existing commercial dilatometer; (*b*) the inverse modeling, novel use of physical constraints, and subsequent numerical simulation software for resolving the proposed model; (*c*) the identification of key thermophysical properties for assuring the minimization of thermal lag in the entire design cell; (*d*) estimation of the average heat transfer coefficient between the sample and the sample holder; and (*e*) the integration of experimental design and analysis for a proper accounting of thermal lags. With these accomplishments, thermal lag in the dilatometer can be understood, quantified, and then minimized. This portion of the project illustrated that the thermal lag associated with thermophysical properties and remote measurements can be accounted for through a method that correlates the measured density to the "true" sample temperature in the melt regime. The results presented here offer insight into the development of an even more improved dilatometer holder, the selection of instrumentation, and the development of a simulation tool that will permit the characterization of high-temperature alloys in the melt regime.

5.3 Technology Transfer

As noted in Section 4.1.6, an additional opportunity arose to validate the results of the modeling and improved experimental procedures from this project. The timely results obtained from this project were successfully applied to the DOE project "Predicting Pattern Tooling and Casting Dimensions for Investment Casting" (DE-FC36-01ID14003) for acquiring optimal thermophysical properties of aluminum alloy A356. These new DSC data resulted in accurate solid fraction measurements that enabled the successful analysis of the investment casting process.

NETZSCH, Inc., one of the manufacturers of instruments used in this project, has expressed interest in this project. The techniques developed in the project were documented in several publications that were also sent to the instrument manufacturers.

All computational and experimental procedures for this project have been published and presented at conferences organized by professional associations. The companies who provided letters of support for this project (Howmet, Inc.; Ford Motor Co.; Flow Science, Inc.; ESI, Inc.; and NETZSCH Instruments, Inc.) have access to the new thermophysical property data generated by this project. The thermophysical properties for aluminum alloy A356 determined by this project were provided to ESI for incorporation into its database, and ESI is currently disseminating this information across industries with its software ProCAST™, a materials property database. New data on additional alloys will be provided to ESI as the information is developed in the future. The supporting companies will also be able to utilize the improved data in their software models.

5.4 Publications and Patents Resulting from Project

This project resulted in numerous conference papers and journal articles reflecting results throughout the project. These are as follows.

1. G. E. Osborne, J. I. Frankel, and A. Sabau, "A New Parameter Estimation Method for DSC Thermodynamic Property Evaluation, Part I: Analytic Developments," presented at the 22nd IASTED International Conference on Modeling, Identification and Control (MIC 2003), Innsbruck, Austria, February 10–13, 2003.

2. G. E. Osborne, J. I. Frankel, and A. Sabau, "A New Parameter Estimation Method for DSC Thermodynamic Property Evaluation, Part II: Runge-Kutta Implementation and Numerical Results," presented at the 22nd IASTED International Conference on Modeling, Identification and Control (MIC 2003), Innsbruck, Austria, February 10–13, 2003.

3. J. I. Frankel and G. E. Osborne, "The Prediction of Heating/Cooling Rates in Material Science Investigations," presented at the 4th International Conference on Quenching and Control of Distortion, Beijing, China, Nov. 23–25, 2003.

4. A. S. Sabau, W. D. Porter, and J. I. Frankel, "Conduction and Radiation Parameters for Analytical Models of Differential Scanning Calorimetry Instruments," presented at TMS 2004, Charlotte, N.C., March 12–14, 2004.

5. G. E. Osborne, J. I. Frankel, and A. S. Sabau, "Characterization of Thermal Lags and Resistances in a Heat-Flux DSC," presented at TMS 2004, Charlotte, N.C., March 12–14, 2004.

6. A. Sabau and W. Porter, "Analytical Models for System Errors of Differential Scanning Calorimetery Instruments," presented at the 2004 ASME Heat Transfer/Fluids Engineering Summer Conference, Charlotte, N.C., July 11–15, 2004.

7. J. I. Frankel, "Motivation for the Development of New Thermal Rate Sensors for Material Science Applications," *International Journal of Materials and Product Technology* (Special Issue: Quenching and Distortion), Invited Paper (to appear).

8. J. I. Frankel, W. D. Porter, and A. S. Sabau, "Analysis of a Modified Push-Rod Dilatometer," *Journal of Thermal Analysis and Calorimetry* (in review).

6. Conclusions

An analytical model was successfully developed for a heat flux DSC instrument. The development of the DSC model was based on actual heat flow paths among the instrument components. This approach can be easily extended to other heat-flux DSC instruments, making it now possible to enhance data acquisition using other DSC instruments. Model parameters were determined using both inverse analysis and direct methods. The final results for pure aluminum and aluminum alloy A356 showed that accurate data on the distribution of the fractional latent heat were obtained with the direct method. The error in thermophysical property data was significantly decreased, from 30% to 3%.

The dilatometer portion of this project demonstrated that use of a careful sample holder design in combination with inverse analysis makes it possible to account for thermal lag in correlating the density to true sample temperature in alloy melts. The results also illustrate that accurate quantification of the sample solid fraction is of critical importance in the analysis portion of the study. This is clearly indicated in Figure 4.20. Thus, instrumentation, sample holder design, inverse analysis, and an accurate model/measurement for the sample solid fraction are required to accurately quantify the density dependence on the true sample temperature. These findings are crucially important for future investigations and for the commercialization of any new sample holder design.

In terms of technology transfer, this project was essentially a feasibility study in which techniques were developed that yield improved thermophysical property data. The demonstrated methodologies are robust and are ready for commercialization. Additional information on technology transfer is presented in Section 5.3, above.

7. Recommendations

7.1 DSC

Additional model development is required in order to obtain accurate data on enthalpy and latent heat distribution. Implementation of the following recommendations will increase the use of these technologies in industry: (*a*) develop a more user-friendly DSC model, and (*b*) install the DSC software on a laboratory system.

7.2 Dilatometer

With additional development, the modified, instrumented sample holder and inverse software could become a viable product. Some issues include enabling rapid sample removal and reinsertion. These issues are well suited for investigation by an interested instrument manufacturer. Reference 32 is a stand-alone report on the dilatometer results and will be presented to interested instrument manufacturers to open a dialogue on future funding and potential usage.

7.3 Technology Transfer

It is desirable to meet with instrument manufacturers and user companies to highlight developments and discuss avenues for implementation. For technology dissemination, it is recommended that a new project be conducted in close collaboration with instrument suppliers and a team of user companies.

8. References

1. M. J. Richardson, "Application of differential calorimetry to the measurement of specific heat," pp. 669–685 in *Compendium of Thermophysical Property Measurement Methods*, vol. 1, ed. K. D. Maglic, A. Cezairliyan, and V. E. Peletsky, Plenum Press, New York, 1984.
2. G. W. H. Hohne and J. E. K. Schawe, "Dynamic behaviour of power compensated differential calorimeters, Part 1: DSC as a linear system," *Thermochmica Acta* 229 (1993): 27–36.
3. G. W. H. Hohne and J. E. K. Schawe, "Dynamic behaviour of power compensated differential calorimeters, Part 2: The signal flow," *Thermochmica Acta* 229 (1993): 37–52.
4. S. W. Chen, C. C. Lin, and C. M. Chen, "Determination of melting and solidification characteristics of solders using differential scanning calorimetry," *Metallurgical and Materials Transactions* A col. 29A (1998): 1965–1972.
5. *Metal Casting Industry Technology Roadmap*, Cast Metal Coalition of the American Foundrymen's Society, January 1998.
6. *Aluminum Industry Technology Roadmap*, The Aluminum Industry, May 1997.
7. *Aluminum Industry Roadmap for the Automotive Market: Enabling Technologies and Challenges for Body Structures and Closures*, The Aluminum Industry, May 1999.
8. *Steel Industry Roadmap,* Steel Industry, 1998.
9. *Glass Technology Roadmap Workshop,* Energetics Inc., Columbia, Md., April 1997.
10. U.S. Department of Energy, Office of Industrial Technologies, Energy Spreadsheet, 2000.
11. *Roadmap for Process Heating Technology,* Industrial Equipment Association and U.S. Department of Energy, Office of Industrial Technologies, March 16, 2001.
12. A. P. Gray, p. 209 in *Analytical Calorimetry*, ed. R. S. Porter and J. F. Johnson, Plenum Press, New York, 1968.
13. S. Jeng and S. Chen, "The solidification characteristics of 6061 and A356 aluminum alloys and their ceramic particle-reinforced composites," *Acta Materialia* 45, no. 12 (1997): 4887–4899.
14. H. B. Dong and J. D. Hunt, "A numerical model of a two-pan heat flux DSC," *Journal of Thermal Analysis and Calorimetry* 64 (2001): 167–176.
15. R. F. Speyer, "Deconvolution of superimposed DTA/DSC peaks using the Simplex algorithm," *Journal of Materials Research* 8, no. 3 (1993).
16. A. T. W. Kempen, F. Sommer, and E. J. Mittemeijer, "Calibration and desmearing of a differential thermal analysis measurement signal upon heating and cooling," *Thermochimica Acta* 383 (2002): 21–30.
17. A. Sabau and W. Porter, "Analytical models for system errors of differential scanning calorimetery instruments," presented at the 2004 ASME Heat Transfer/Fluids Engineering Summer Conference, Charlotte, N.C., July 11–15, 2004.
18. G. E. Osborne, J. I. Frankel, and A. Sabau, "A new parameter estimation method for DSC thermodynamic property evaluation, part I: Analytic developments," presented at the 22th IASTED International Conference on Modeling, Identification and Control (MIC 2003), Innsbruck, Austria, February 10–13, 2003.

19. G. E. Osborne, J. I. Frankel, and A. S. Sabau, “Characterization of thermal lags and resistances in a heat-flux DSC,” presented at TMS 2004, Charlotte, N.C., March 12–14, 2004.

20. J. V. Beck, B. Blackwell, and C. R. St. Clair, *Inverse Heat Conduction*, Wiley and Sons, New York, 1985.

21. K. Kurpisz and A. J. Nowak, *Inverse Thermal Problems*, Computational Mechanics, United Kingdom, 1995.

22. D. M. Trujillo and H. R. Busby, *Practical Inverse Analysis in Engineering*, CRC Press, Boca Raton, Fla., 1997.

23. J. I. Frankel and M. Keyhani, “A global time treatment for inverse heat conduction problems,” *Journal of Heat Transfer* 119 (1997): 673–683.

24. J. I. Frankel, unpublished notes and computer codes, 2001–2003.

25. A. S. Carasso, “Space marching difference schemes in the nonlinear inverse heat conduction problem,” *Inverse Problems* 8 (1992): 25–42.

26. J. I. Frankel, M. Keyhani, and K. Taira, “In-phase error estimation of experimental data and optimal first derivatives,” *AIAA Journal* 42, no. 5 (2004): 1017–1024.

27. J. G. Hust, *Standard Reference Materials: A Fine-Grained, Isotropic Graphite for Use as NBS Thermo-physical Property RM's from 5 to 2500 K,* NBS Special Publications 260-89, National Bureau of Standards, Washington, D.C., 1984.

28. W. Kaplan, *Advanced Calculus*, Addison-Wesley, Reading, Mass., 1973.

29. R. L. Hardy, “Theory and applications of the multiquadratic biharmonic method,” *Computers and Mathematics with Applications* 19 (1990): 163–208.

30. Auburn University Materials Processing Center Materials Database, online at http://metalcasting.auburn.edu/data.

31. D. M. Stefanescu, *Science and Engineering of Casting Solidification*, Kluwer, New York, 2002.

32. J. I. Frankel, W. D. Porter, and A. S. Sabau, “Analysis of a modified push-rod dilatometer,” *Journal of Thermal Analysis and Calorimetry* (in review).